

Physics-Based Image Segmentation Using First Order Statistical Properties and Genetic Algorithm for Inductive Thermography Imaging

Bin Gao¹, Senior Member, IEEE, Xiaoqing Li, Wai Lok Woo, Senior Member, IEEE, and Gui Yun Tian, Senior Member, IEEE

Abstract—Thermographic inspection has been widely applied to non-destructive testing and evaluation with the capabilities of rapid, contactless, and large surface area detection. Image segmentation is considered essential for identifying and sizing defects. To attain a high-level performance, specific physics-based models that describe defects generation and enable the precise extraction of target region are of crucial importance. In this paper, an effective genetic first-order statistical image segmentation algorithm is proposed for quantitative crack detection. The proposed method automatically extracts valuable spatial-temporal patterns from unsupervised feature extraction algorithm and avoids a range of issues associated with human intervention in laborious manual selection of specific thermal video frames for processing. An internal genetic functionality is built into the proposed algorithm to automatically control the segmentation threshold to render enhanced accuracy in sizing the cracks. Eddy current pulsed thermography will be implemented as a platform to demonstrate surface crack detection. Experimental tests and comparisons have been conducted to verify the efficacy of the proposed method. In addition, a global quantitative assessment index F-score has been adopted to objectively evaluate the performance of different segmentation algorithms.

Index Terms—Thermography, non-destructive testing and evaluation, image segmentation, genetic functionality, F-score.

I. INTRODUCTION

IN CONTRAST to conventional NDT&E methods [1]–[4], infrared thermography (IRT) offers prominent advantages which include abilities to inspect over a large detection area within a short interval and provides capabilities of contactless as well as high spatial resolution [5], [6]. Research on non-destructive testing (NDT) methods for fatigue crack detection

has begun over the last 100 years. Magnetic Particle Testing (MT) is effective for detecting surface and near surface discontinuities. This technique has been widely adopted in industry. However, the MT testing is augmented with complicated detection process. The surface of the sample requires pretreatment and the measurement consumes relatively long duration. In addition, it pollutes the environment. IRT is applicable to a wide range of materials, including composites and metallic materials [7]. IRT is generally divided into two major groups: passive infrared thermography (PIT) and active infrared thermography (AIT) [8]. ECPT is an AIT technique developed to provide accurate information by considering the amount of thermal radiation and heat transfer for conductive material. ECPT has potential to replace MT technique due to its rapid inspection over a large area and sensitivity with near surface defects [9], [10]. In the presence of defect, the resultant eddy current will be distorted and the heat shows an abnormal expression that increases the temperature contrast between the defective region and defect-free areas. In previous work, ECPT has been used for damage detection in metallic alloy [11], carbon fiber reinforced plastic [12] and crack detection of rolling contact fatigue of rail tracks [13]. Our previous study reported an unsupervised feature extraction algorithm on ECPT for automatic pattern separation [14]. He et al. used time-to-peak feature for wall thinning and inner defects characterization [15]. Liu *et al.* proposed the thermo-optical flow entropy tracking method to trace the heat flow and characterize the degree of fatigue damage [16].

Image segmentation aims to separate the desired foreground object from background [17]. These segmentation methods are usually classified into four major categories: threshold-based, region growing, edge detection, and hybrid methods [18]. Stelios [19] proposed a local search based on genetic sequential image segmentation algorithm for the classification of remotely sensed images. Sanchez *et al.* [20] improved the parameters selection for an automatic multiband image segmentation on the basis of a seeded region growing-merging approach. Liu *et al.* [21] presented an efficient multiscale low rank representation for image segmentation. Jian and Jung [22] presented interactive image segmentation by using adaptive constraint propagation (ACP) for semantic segmentation. Wang and Huang [23] proposed the eigen-decomposition of an anisotropic diffusion operator for image segmentation. Hell *et al.* [24] reported an approach to fast multi-label color image segmentation by using convex optimization techniques. Wang *et al.* [25] discussed a novel sparse global/local affinity graph over superpixels of an input image to capture both short- and long-range

Manuscript received July 4, 2016; revised April 12, 2017, September 18, 2017, and November 20, 2017; accepted December 4, 2017. Date of publication December 14, 2017; date of current version February 9, 2018. This work was supported in part by the National Natural Science Foundation of China under Grant 61401071 and Grant 61527803, in part by NSAF under Grant U1430115, and in part by EPSRC IAA Phase 2 through the 3D Super-Fast and Portable Eddy Current Pulsed Thermography for Railway Inspection Project under Grant EP/K503885/1. The associate editor coordinating the review of this manuscript and approving it for publication was Dr. Christos Bouganis. (*Corresponding author: Bin Gao.*)

B. Gao, X. Li, and G. Y. Tian are with the School of Automation Engineering, University of Electronic Science and Technology of China, Chengdu 610051, China (e-mail: bin.gao@ncl.ac.uk).

W. L. Woo is with the School of Electrical, Electronic and Computer Engineering, Newcastle University, Newcastle upon Tyne NE1 7RU, U.K.

Color versions of one or more of the figures in this paper are available online at <http://ieeexplore.ieee.org>.

Digital Object Identifier 10.1109/TIP.2017.2783627

grouping cues. Liu *et al.* [26] proposed an unsupervised FCM-based image segmentation method by paying closer attention to the selection of the local information. El-Zehiry and Grady [27] provided a contrast driven elastic model which can accommodate high curvature objects. Dong and Shen [28] presented a novel sub-Markov random walk algorithm with label prior for seeded image segmentation. Li *et al.* [29] proposed a segmentation approach to automatically detect cracks from magnetic tile images by using the fast discrete Curvelet transform. Li *et al.* [30] provided an image layering and confidence analysis for small target detection in infrared image. Świta and Suszyński [31] introduced optimization methods to K-means segmentation algorithm for thermal images. Huang and Wu [32] employed the multilayer level set method to segment infrared thermal image for layered structures defect of carbon fiber reinforced plastic (CFRP).

In reviewing the current defect detection methods for ECPT, two major challenges have been identified. Firstly, there is a lack of capability in automating the detection and identification of cracks. Secondly, the need to improve the detectability and enhance the resolution of small cracks. The latter is the main point of achieving Quantitative NDT&E. However, most recent methods are limited to manual selection of the contrastive components. The results are acceptable but generally not predictable. The proper contrastive components have to be empirically selected. In addition, there is a lack of appropriate segmentation algorithm that takes into account the physics behavior of defects in inductive thermography. This ambiguous case prevents the use of inductive thermography imaging in automated environments. Thus, automated image segmentation for crack separation is crucially required for ECPT. This paper proposes a new method that incorporates the physics characteristics of defect behavior in IRT to derive the first order statistical properties (FOSP) of defect segmentation and utilizes the genetic algorithm to automatically adapt the statistical features for further optimization of the threshold selection. The proposed method has consistent performance and strong de-noising capability. The comparison in terms of the F-score has been undertaken for different segmentation algorithms through the real experiments. Experimental tests on man-made metal defects and natural defects have been conducted to show the validity of the proposed algorithm.

The remainder of this paper is organized as follows: Firstly, the introduction of methodology and the proposed method are presented in Section II. The results and discussion are presented in Section III. Finally, conclusions and further work are drawn in Section IV.

II. METHODOLOGY

A. Image Segmentation Methods (ISMs)

Three typical ISMs based on threshold approach are briefly presented. These include maximum between-class variance (BCV or Otsu) [33], Iterative thresholding (IT) [34], and Hamadani [35], segment the target from the background by using a certain threshold. Generally, let the original image be denoted as $I(x, y)$, then the segmented image $G(x, y)$ is defined as:

$$G(x, y) = \begin{cases} 1 & \text{if } I(x, y) > T \\ 0 & \text{if } I(x, y) \leq T \end{cases} \quad (1)$$

where T is the threshold value. As for Otsu, the optimum threshold is obtained by determining the BCV of the foreground and background, which is given by

$$T_{opt} = \arg \max_T \left\{ \frac{P(T)[1 - P(T)][\mu_f(T) - \mu_b(T)]^2}{P(T)\sigma_f^2(T) + [1 - P(T)]\sigma_b^2(T)} \right\} \quad (2)$$

where μ_b and μ_f represent the mean value of the image background and foreground, respectively. σ_b and σ_f are the standard deviation for the background and foreground of the image, respectively. $P(T)$ expresses the cumulative probability which is defined as:

$$P(T) = \sum_{i=0}^T p(i) \quad \text{where } p(i) = \frac{n_i}{N} \quad (3)$$

where n_i is the frequency of pixel value i , N is the total number of pixels in the image, and $p(i)$ is the probability of each pixel value.

Iterative thresholding (IT) adopts an iterative approximation by which automatic threshold choice is accomplished. The maximum (T_{max}) and the minimum (T_{min}) pixel values are firstly found in an image, and the initial threshold (T_k) is set as $(T_{max} + T_{min})/2$. According to T_k , the image is divided into the background and foreground, namely

$$T_1 = \frac{\sum_{z(i,j) < T_k} z(i,j) \times N(i,j)}{\sum_{z(i,j) < T} N(i,j)} \quad T_2 = \frac{\sum_{z(i,j) > T_k} z(i,j) \times N(i,j)}{\sum_{z(i,j) > T} N(i,j)} \quad (4)$$

where $z(i, j)$ is the pixel value of the point (i, j) , $N(i, j)$ indicates weight coefficient of pixel (i, j) . The total number of pixel is a , the number of pixel with $z(i, j)$ is b , $N(i, j)$ is equal to b/a . Subsequently, a new threshold is determined, i.e. $T_{k+1} = (T_1 + T_2)/2$. If $T_k = T_{k+1}$, the method puts an end, otherwise, $k + 1 \rightarrow k$, T_{k+1} is taken as a new T_k , the reclassification is implemented according to the Eqn. (6) until $T_k = T_{k+1}$.

The threshold determination according to Hamadani is given as follows:

$$T = k_1 \times \mu + k_2 \times \sigma \quad \text{where } \mu = \frac{1}{M \times N} \sum_{x=1}^M \sum_{y=1}^N I(x, y),$$

$$\sigma = \sqrt{\frac{1}{M \times N} \sum_{x=1}^M \sum_{y=1}^N (I(x, y) - \mu)^2} \quad (5)$$

where μ represents the mean of the image, σ indicates the standard deviation for the image, k_1 and k_2 are the constants. In this work, the value of k_1 and k_2 are set as 1 and 1.5, respectively. In addition, the size of the image is $M \times N$.

K-means algorithm [36] is a commonly used image segmentation method. Suppose that an image X contains K clusters: X_1, X_2, \dots, X_K . The sample number (pixel number) in each cluster: n_1, n_2, \dots, n_k . The mean of each cluster is represented as the cluster center: m_1, m_2, \dots, m_k . The implementation of K-means is as follows:

- i) All pixels are randomly assigned to K clusters to initialize each cluster, and calculating the average of each cluster to initialize the cluster center;

- ii) The pixels in each cluster are assigned to the nearest cluster according to the minimum distance principle. Euclidean distance is described as:

$$d(x, m_i) = \sqrt{(p - m_i)^2}, \quad \text{where } (i = 1, 2, \dots, k),$$

$$p \in X_i \quad (6)$$

- iii) Calculating the mean of each new cluster as a new cluster center;
v) Calculating the sum of squares of errors:

$$E = \sum_{i=1}^k \sum_{p \in X_i} \|p - m_i\|^2 \quad (7)$$

- vi) repeating ii)~v) until the sum of squares of errors is the optimally least. In our work, cluster is set as 2.

In addition, a seeded region growing (RG) method is used for comparison. The details of the method can be found in [37].

B. Proposed FOSP-GA Method

1) *Physics-Pattern Model of Inductive Thermography*: The infrared camera records both the spatial and the transient response of temperature variation of the specimen. This can be represented as a spatial-transient tensor \bar{Y} , which has dimension $\underbrace{N_x \times N_y}_{\text{Spatial}} \times \underbrace{N}_{\text{Transient}}$. According to Maxwell's equations,

the theory of the electromagnetic (EM) field in the ECPT system can be deduced. When an EM field is applied to a conductive material, the temperature increases owing to resistive heating from the induced eddy current which is known as the Joule heating. The sum of the generated resistive heat Q is proportional to the square of the magnitude of the electric current density. Current density, in turn, is proportional to the electric field intensity vector \vec{E} . The following equation expresses this relationship:

$$Q = \frac{1}{\sigma} |\vec{J}_s|^2 = \frac{1}{\sigma} |\sigma \vec{E}|^2 \quad \text{where } \sigma = \frac{\sigma_0}{1 + \alpha(T - T_0)} \quad (8)$$

σ is dependent on temperature, and σ_0 is the conductivity at the reference temperature T_0 and α is the temperature coefficient of resistivity, which describes how resistivity varies with temperature. In general, by taking account of heat diffusion and Joule heating [37], the heat conduction equation of a specimen can be expressed as:

$$\frac{\partial T}{\partial t} = \frac{k}{\rho C_p} \left(\frac{\partial^2 T}{\partial x^2} + \frac{\partial^2 T}{\partial y^2} + \frac{\partial^2 T}{\partial z^2} \right) = \frac{1}{\rho C_p} q(x, y, z, t) \quad (9)$$

where $T = T(x, y, z, t)$ is the temperature distribution, k is the thermal conductivity of the material (W/m K), which is dependent on temperature. ρ is the density (kg/m³), C_p is specific heat (J/kg K). $q(x, y, z, t)$ is the internal heat generation function per unit volume, which is the result of the eddy current excitation. From the above analysis, it becomes clear that the variation of temperature spatially and its transient response directly reveals the intrinsic properties variation of the conductive material.

In order to pave the way to interpreting the physics characteristics of the defect behavior, the system of ECPT is firstly shown in Fig. 1. The excitation signal generated by the excitation module is a small period of high frequency current.

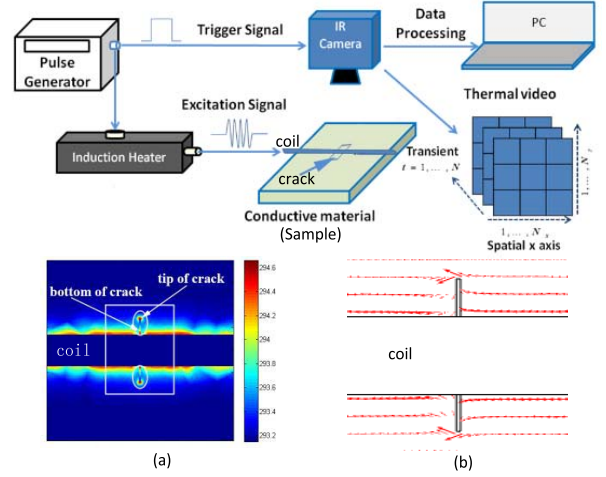


Fig. 1. Inductive Thermography and interpretation of defect behavior.

The current in the coil will induce the eddy current and generate the resistive heat in the conductive material. If a defect exists, the distribution of eddy current (EC) and thermal diffusion will be disturbed. Specifically, when the EC encounters a discontinuity, e.g. crack, it will be forced to divert, leading to an increase of the EC density within the vicinity of the defect as shown in Fig. 1(b). The arrow indicates the direction of the EC while the length of the arrow represents the EC intensity. Fig. 1(a) shows the numerical simulations for the fusion of eddy current and temperature distribution which are performed using COMSOL Multi-physics simulation software. The distribution of the EC in Fig. 1(a) as marked by a rectangle area is shown in Fig. 1(b). Consequently, this will lead to variation in the resultant surface heat spatial distribution and the transient response of temperature. These variations are captured by an infrared camera. For surface crack, prominent features can be observed at both tip and bottom of the crack, as shown in Fig. 1(a). Once the prominent features of the crack are extracted, then the location of the crack can be readily identified and quantified.

2) *Physics-Based Interpretation of Crack Behavior*: Based on the above analysis of physics characteristics of the defect behavior in inductive thermography, it can be readily inferred that defect areas radiate more heat than background area. This indicates that the defect preserves large amount of energy, and is located at the top-end of the image histogram. In order to obtain specific defect status from the histogram as *a priori* information for image segmentation, the defect thermal images will be tested and analyzed.

It should be noted that the thermal image contains only one waveband, i.e. the infrared waveband. Therefore, the adopted thermal image is the pseudo color image. In order to analyze the data, Fig. 2(a) is mapped directly to the histogram without data transformation and compression, as shown in Fig. 2(b). The distribution of real temperature values is then mapped into the digital level of the histogram in Fig. 2(b). The radiation of the object was sampled by using the commercial thermography software Altair and the unit of radiation is digital level (DL). A nonlinear transfer function after calibration can convert the radiation (unit: DL) into temperature (unit: K/°), which requires an operator setting several parameters such as emissivity background temperature, and transmission. In order to simplify the process, we used DL as the representation of temperature in the experiment.

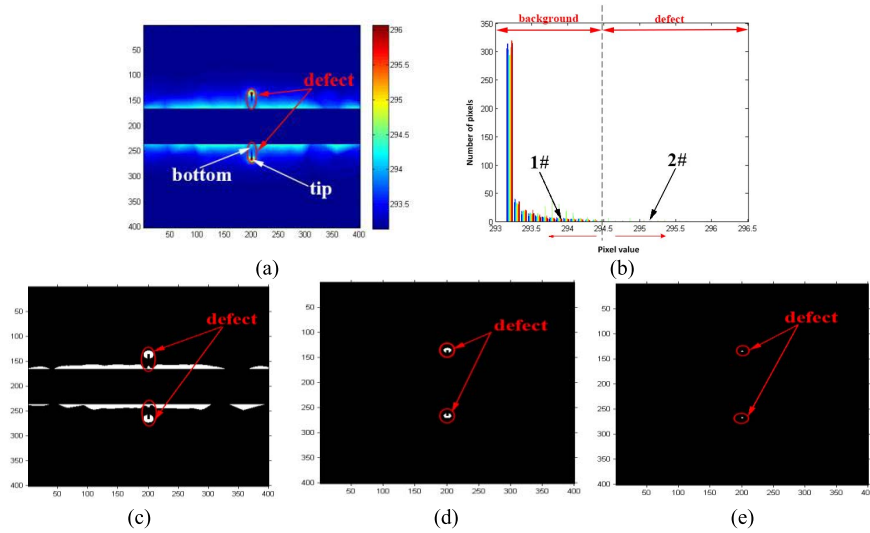


Fig. 2. (a) Crack thermal image at 0.04s; (b) histogram of (a); (c) segmentation result of (a) at position 1#; (d) segmentation result of (a) on the dotted line; (e) segmentation result of (a) at position 2#.

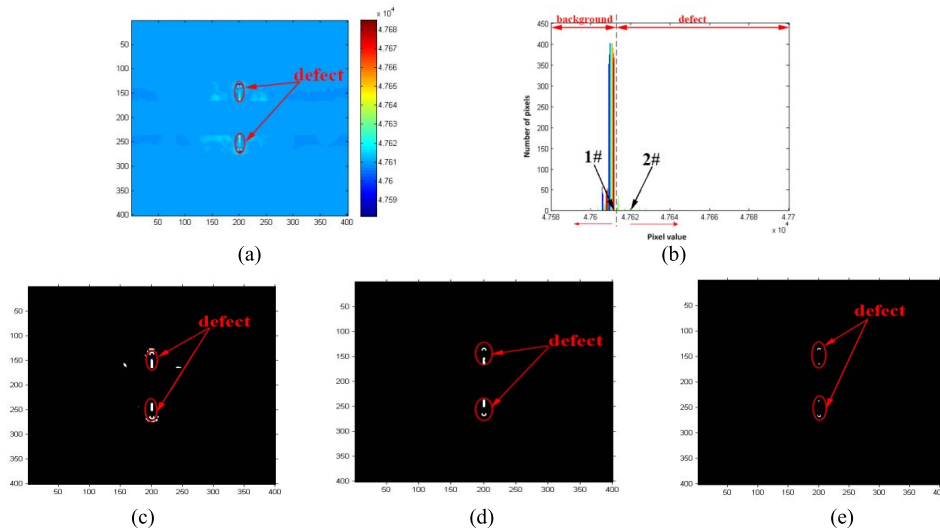


Fig. 3. (a) ICA thermal pattern; (b) histogram of (a); (c) segmentation result of (a) at position 1#; (d) segmentation result of (a) on the dotted line; (e) segmentation result of (a) at position 2#.

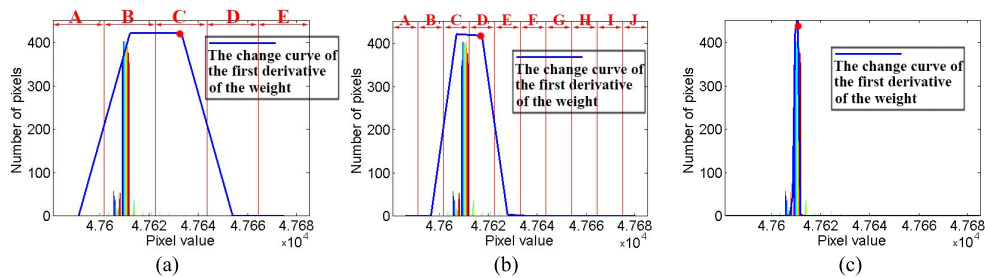


Fig. 4. Histogram with various groups: (a) histogram is equally divided into 5 groups, (b) histogram is equally divided into 10 groups, (c) histogram is equally divided into 100 groups.

Fig. 2(a) illustrates the simulation result for surface crack at 0.04s, which is the early response of eddy current heating and has the largest contrast between defective and non-defective area. The segmentation result by manually selecting the threshold on the dotted line of Fig. 2(b) is displayed in Fig. 2(d). This selection is based on the Monte Carlo approach where the process is repeated over 10 times. The result shows that the

background and the defect are optimally separated. However, when the threshold is located on the left side of the dotted line in Fig. 2(b), such as the selection threshold at position 1#, unwanted background information is included. This can be seen in Fig. 2(c). When the threshold is located on the right side of the dotted line (such as position 2#), the result shows the worse performance of defect segmentation. According to

Fig. 2(c)-(e), it can be seen that threshold falls on the right of the dotted line in Fig. 2(b) can be expected to render a good segmentation result. Otherwise, the segmented image will contain background interference. The same case is illustrated in Fig. 3.

However, by comparing Fig. 2(c)-(e) and Fig. 3(c)-(e), it is indicated that more defect information is retained in Fig. 3(c)-(e). This benefit comes from the contribution of preprocessing of Independent Component Analysis (ICA). ICA [14] has the capability to automatically extract the spatial and temporal information of defects according to the whole thermography sequence without any training knowledge. This process avoids the issue of manual selection of the specific thermal frame. Generally, the 3~6 independent components can be used to describe the main information contained in the whole thermography sequence. In addition, the independent component with the maximum kurtosis contains significant defect information and this is adopted as the pre-segmented image. Thus, the ICA is used as a pre-processing method for the original thermography sequence, as shown in Fig. 3(a). Simultaneously, in order to analyze the ICA data, Fig. 3(a) is mapped to the histogram without the data transformation and compression, this is shown in Fig. 3(b).

3) *Derivation of FOSP-GA Method*: It is hypothesized that the defect and background could be effectively separated by selecting an optimal threshold boundary, as the illustrated by the dotted line in Fig. 3(b). The optimal defect segmentation result can be obtained by using the threshold that falls into the appropriate boundary of the defect related histogram range.

In order to effectively separate the defect from the background, this paper considers the strategy that 1) divides the histogram equally into multiple groups and 2) performs automatic threshold selection for separation. The mean pixel value of each group is used as a candidate boundary and threshold. The total number of pixel in each group represents the weight. The rate of change of the weight is computed by calculating the first order derivative, and the maximum elbow point is taken as an alternation of the weight to distinguish the defect and background. The proposed strategy is to adaptively seek a threshold boundary to maximally distinguish the defect from the background. Taking Fig.3(b) as an example, Fig. 4 illustrates the histogram partition into 5, 10 and 100 groups, respectively.

Based on the above analysis, a new FOSP-GA method is proposed on the basis of a combination of the first order statistical properties (FOSP) with genetic algorithm (GA). The proposed method combines the genetic functionality with the FOSP to automatically control the segmentation threshold so as to render better accuracy in locating as well as sizing the defect.

4) *Proposed FOSP-GA Algorithm*: Concerning the statistical characteristics, the histogram shows the distribution of the pixel number for each different pixel value. With regard to the FOSP, the histogram is equally divided into n groups ($n \geq 2$) and the width of each group is calculated as follows:

$$\Delta V = \frac{V_{\max} - V_{\min}}{n} \quad (10)$$

where V_{\max} and V_{\min} are maximum and minimum value of the pixel in the image, respectively. Subsequently, V_i can be defined as:

$$V_i = V_{\min} + i \times \Delta V, \quad (i = 0, 1, 2, \dots, n) \quad (11)$$

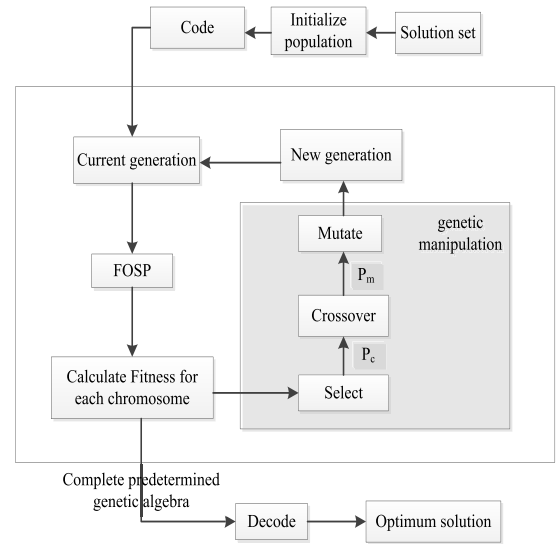


Fig. 5. Flow diagram of the proposed FOSP-GA. (Note: MATLAB® demo code of the proposed method can be found in <http://faculty.uestc.edu.cn/gaobin/en/lwcz/153408/list/index.htm>)

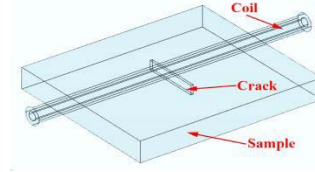


Fig. 6. 3D simulation model.

Each group can be specifically expressed as: $V_0 \sim V_1$, $V_1 \sim V_2, \dots, V_{n-1} \sim V_n$, i.e., $V_i \sim V_{i+1}$. The next step is accumulating the corresponding pixel number u_v of pixel value v that falls within $V_i \sim V_{i+1}$ and calculating the average pixel value of each group:

$$S_i = \sum_{V_{i-1} < v < V_i} u_v, \quad W_i = \frac{\sum_{V_{i-1} < v < V_i} v \times u_v}{S_i}, \quad (i = 1, 2, \dots, n) \quad (12)$$

where W_i denotes average pixel value of each group, that is, a candidate boundary of defect and background. S_i demonstrates the weight of each group. Obviously, it is a discrete model and the first order derivative of S_i is computed as follows:

$$k_i = S_i - S_{i-1}, \quad (i = 1, 2, \dots, n. \text{ where } S_0 = 0) \quad (13)$$

The maximum absolute value of k_i is searched and this is denoted as k_{\max} . The term k_{\max} is considered as an alternation of weight for the distinction of the defect and background. Owing to the target which distributes in the top-end of the histogram, the right side of k_{\max} is taken as the target area. If i is equal to n , threshold T was determined as W_n , otherwise, T is W_{i+1} . Accordingly, the threshold determination can be achieved.

However, the non-optimized selection of the different grouping number for histogram indirectly introduces unwanted interference to the determinations of both k_{\max} and T . In order to search for a suitable quantity of division, genetic algorithm (GA) is incorporated into FOSP. GA is firstly proposed by Goldberg and Holland [38], which has traced the procedure of evolution of stochastic global parallel search algorithm.

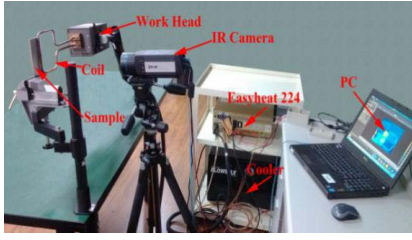


Fig. 7. Experiment setup.

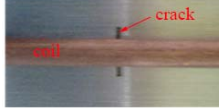


Fig. 8. Test specimen.

TABLE I

ELECTRICAL AND THERMAL PARAMETERS FOR STAINLESS STEEL

Parameters	Steel
Conductivity (S/m)	1.369863×10^6
Relative permeability	1
Density(kg/m^3)	7980
Heat capacity($\text{J}/(\text{kg} \times \text{K})$)	502
Thermal conductivity($\text{W}/(\text{m} \times \text{K})$)	12.1
Thermal diffusivity(m^2/s)	3.020499×10^{-6}

It has strong robustness and global optimization performance. The strategy is internally built into FOSP where the core process is shown in Fig. 5. The specific description can be summarized as follow:

- (i) *Code and initialize population*: chromosomes are generated by binary code which represent all solutions. In the work, an upper limit of 256 bins is sufficient for the FOSP in processing the inductive thermal image. Therefore the quantity of division of the histogram can be represented as 8 bit binary, i.e. a chromosome. The procedure is creating the initial population with chromosomes randomly sampled from an independent and identically distributed library. The creation should be neither too large nor small. Otherwise, this leads to the slow convergence speed or non-optimal solution. In this work, 10 chromosomes are set as the initial population, and the encoded initial population serves as the current generation.
- (ii) *FOSP and Fitness function*: A fitness function is defined to evaluate each chromosome where the greater the value, the stronger the ability to survive. In our work, image entropy is chosen as fitness function:

$$H = \sum_{i=0}^n p_i \log p_i \quad (14)$$

where p_i represents the frequency of pixel value i in the image. Image entropy denotes that aggregation of the pixel value distribution, which reflects the average information of the image. For inductive thermal images, the number of pixels in the defect is few relative to the whole image, that is, the defect is small and has sparse characteristic. Therefore, the larger the entropy, the better the segmentation result. Since entropy is a measure of certainty, the entropy has been selected as the fitness function.

- (iii) *Selection of genetic seed*: For the fitness of each chromosome, the fine chromosome is inherited to the next population. In our work, the rule is selected that the chromosomes of the current population are randomly replaced by chromosomes in last population whose fitness value is greater than those of the current population.
- (iv) *Crossover*: Crossover refers to some bits of the two chromosomes are exchanged in the current population, and cross-operation is implemented based on crossover probability (P_c) to generate a new population. The greater the crossover probability, the more bits (i.e. genes) are exchanged, and the faster the convergence rate of the solution. However, a large crossover probability is unfavorable for determining an optimal solution for values $0.4 \sim 0.9$ are considered. Here the crossover probability is set as 0.4.
- (v) *Mutate*: On the basis of mutation probability (P_m), some bits of chromosomes in the current population are changed from 1 to 0, or 0 to 1, and the new generation is formed. It is important to note that if P_m exceeds 0.5 GA can suffer from inferior optimization ability. Here, the mutation probability is set as 0.3.
- (vi) *Regenerate*: After the genetic operation, a new population is generated. The current generation covers the last generation. In addition, the new generation is set as the current generation, and then go to ii).
- (vii) *Genetic algebra*: The program selects a genetic algebra as the determined conditions of termination for the optimization loop. When algorithm has progressed a certain generation, the optimal solution can be obtained and ordinarily the genetic algebra is selected as $50 \sim 500$. In our work, in order to ascertain the convergence of the solution, the genetic algebra is set as 50. When a predetermined genetic algebra is completed, the chromosome with largest fitness is selected as the best result that is decoded as the inverse process of encoding. All the above parameter settings are validated by using Monte-Carlo repeated experiments involving more than 20 independent trials in order to obtain robust results.

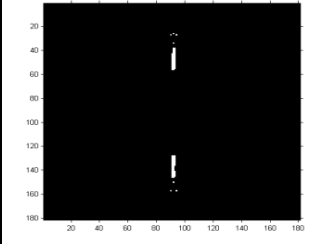
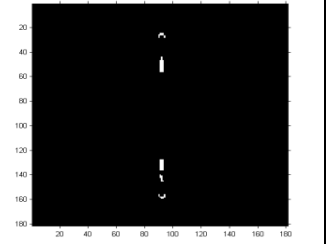
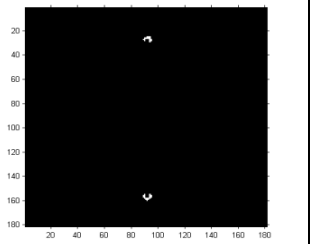
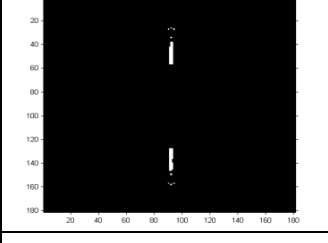
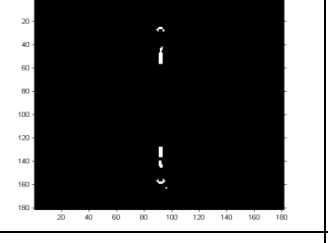
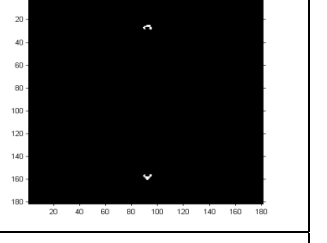
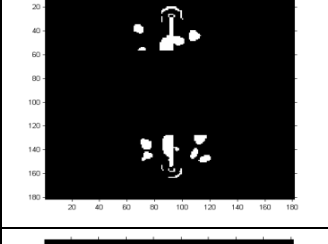
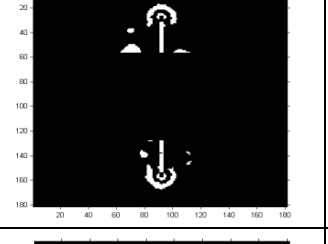
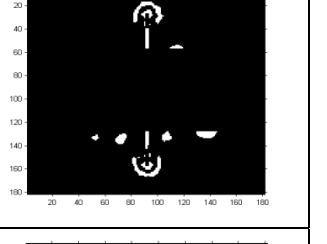
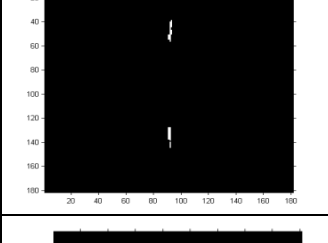
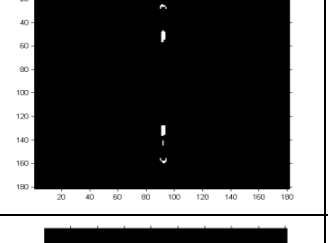
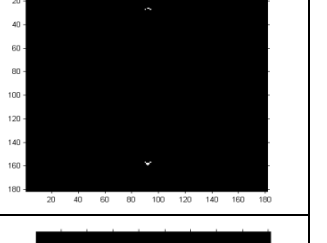
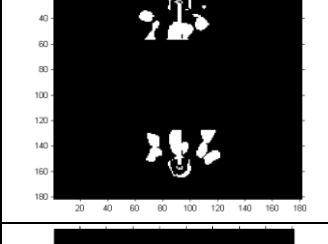
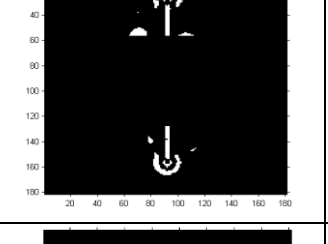
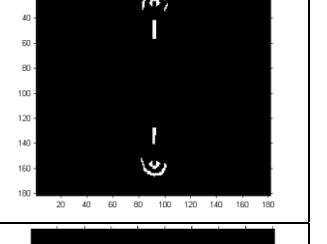
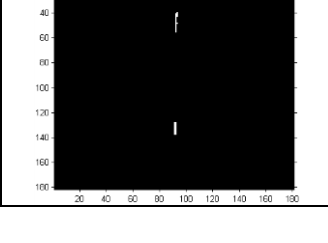
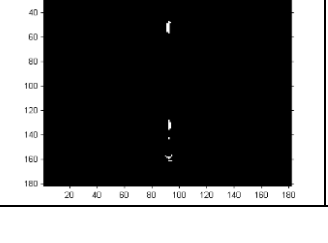
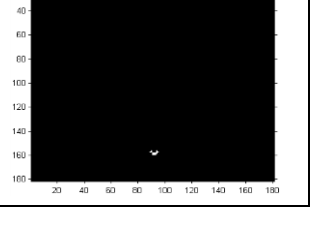
C. Quantitative Detectability Assessment

Non-destructive evaluation involves the measurement of complex parameters with inherent variations in both the measurement process and part under test. The output from such a measurement decision process can be analysed as a problem in conditional probability. The outcome can be classified into the following four results: True positive (TP): a defect exists and is detected; False positive (FP): no defect exists but one is identified; False negative (FN): a defect exists but is not detected; True negative (TN): no defect exists and none is detected. Both TP and FN outcomes represent the total opportunities for positive calls (effective number of defects) while both FP and TN outcomes represent the total opportunities for false alarms (effective number of no defects). Thus, the precision and recall can be defined as:

$$\text{Precision} = \frac{TP}{TP + FP} \quad \text{Recall} = \frac{TP}{TP + FN} \quad (15)$$

The desired results of the application of NDE procedures are defect detection (signal present) or signal non-detection (signal absent). In order to balance the judgement of precision and

TABLE II
SEGMENTATION RESULTS OF VARIOUS METHODS IN THE SIMULATION

	TP I	TP II	TP III
Otsu			
IT			
Hamadani			
FOSP-GA			
K-Means			
RG			

recall, F-score is used as a measure of test accuracy, namely:

$$F = \frac{(\alpha^2 + 1) \times \text{Precision} \times \text{Recall}}{\alpha^2(\text{Precision} + \text{Recall})} \quad (16)$$

where α is a default value that relates weight the Precision and Recall, weightage. In this paper, α is equal to one that means Recall is as important as Precision.

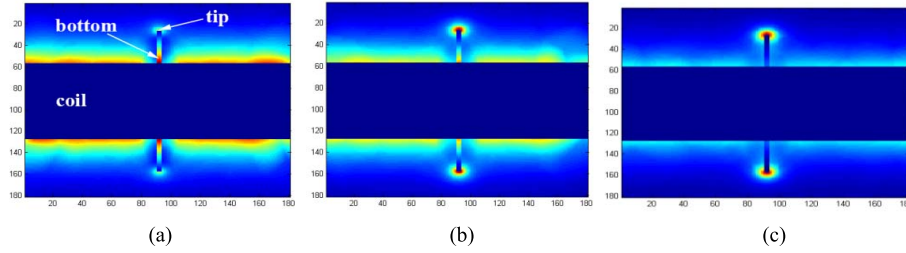


Fig. 9. (a)-(c) The thermal patterns of crack in the simulation.

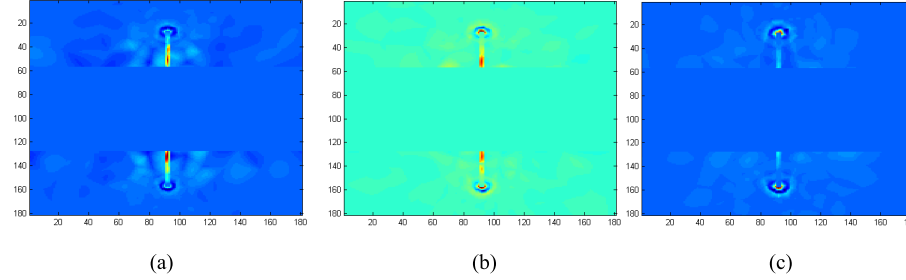


Fig. 10. (a)-(c) The corresponding pre-segmented images of Fig. 12(a)-(c).

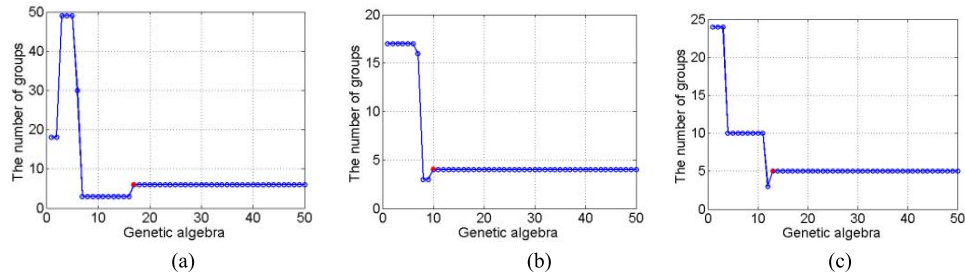


Fig. 11. (a)-(c) Evolution curve of FOSP-GA for TP I, II, III, respectively.

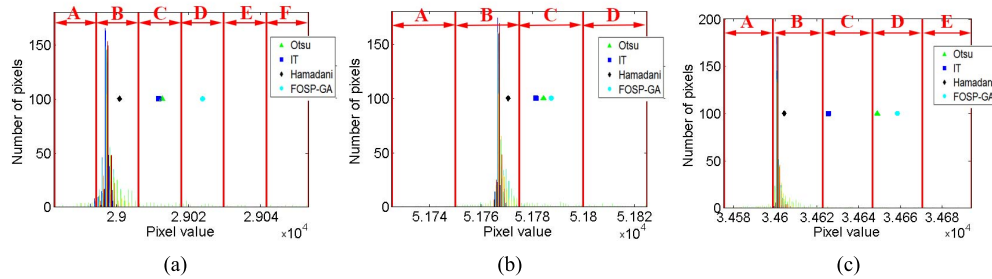


Fig. 12. (a)-(c) Histogram for TP I, II, III, respectively.

TABLE III
F-SCORE FOR VARIOUS ISMs IN THE SIMULATION

method	simulation			
	TP I	TP II	TP III	average
Otsu	0.8628	0.9714	0.9524	0.9289
IT	0.8732	0.9668	0.9581	0.9327
Hamadani	0.5299	0.6126	0.5844	0.5756
K-Means	0.4823	0.6321	0.6871	0.6005
RG	0.8512	0.9610	0.9513	0.9212
FOSP-GA	0.8438	0.9752	0.9874	0.9355

In inductive thermography the main objective is to automatically extract the tips and bottoms of the cracks, which is sufficient to identify the defects as well as quantitatively perform the measurement.

III. RESULTS AND DISCUSSION

A. Sample Preparation and Experiments 4Setup

Numerical simulation was performed by using COMSOL Multiphysics simulation software via the electro-thermal

module combined with the application mode. Fig.6 shows the construction of the model. The electrical and thermal parameters for the 304# stainless steel used in the simulation are displayed in Table I. A line inductor with an outer radius of 3.5mm and inner radius of 2.5mm was modelled on experimental coil used in the test and is positioned perpendicular to the sample.

The experimental set-up is shown in Fig. 7. In the experiment, only one edge of the rectangular coil is used to stimulate eddy current to the underneath sample, and placed in the middle of the crack (see Fig. 8). In this study, the frame rate of 100 Hz is chosen, 380 A_{rms} and 256 kHz are used, and 200 millisecond videos are recorded in the experiments.

B. Performance Analysis and Evaluation of Different Image Segmentation Methods

1) *Simulation Analysis:* For crack detection, three typical thermal patterns (TPs) can be observed. These are (i) thermal information is more significant than that at the tip (see Fig. 9(a)); (ii) thermal information of both crack tips and

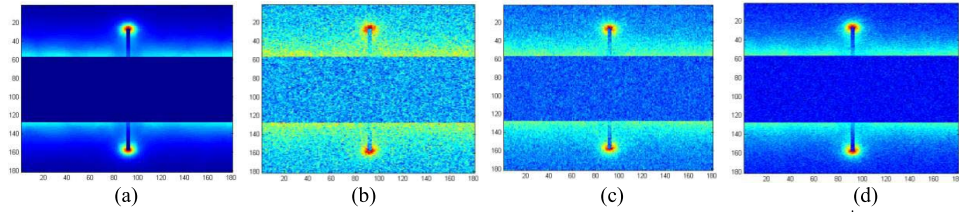


Fig. 13. (a) pre-segmented image; (b)-(d) pre-segmented images with white noise of 0dB, 5dB and 10dB, respectively.

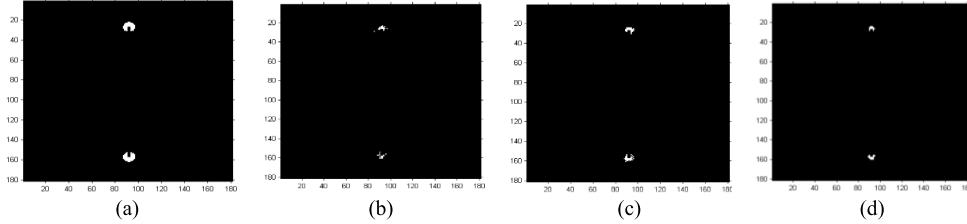


Fig. 14. (a) segmentation result by FOSP-GA of pre-segmentation image; (b)-(d) segmentation results by FOSP-GA of pre-segmented image with white noise of 0dB, 5dB and 10dB, respectively.

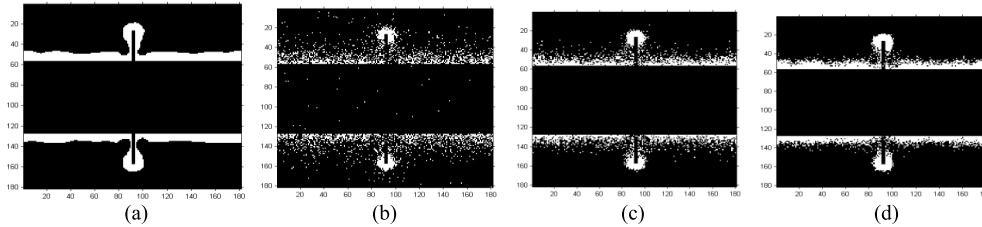


Fig. 15. (a) segmentation result by Hamadani of pre-segmented image; (b)-(d) segmentation results by Hamadani of pre-segmented image with white noise of 0dB, 5dB and 10dB, respectively.

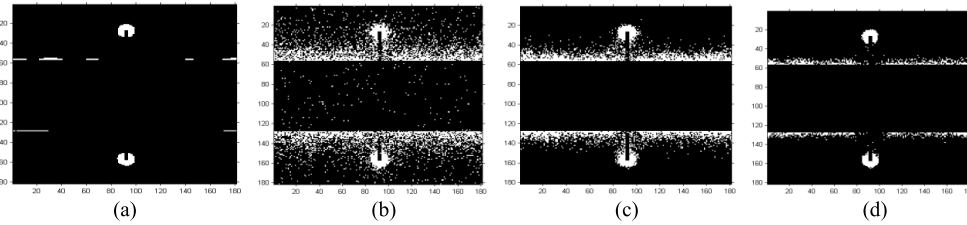


Fig. 16. (a) segmentation result by IT of pre-segmented image; (b)-(d) segmentation results by IT of pre-segmented image with white noise of 0dB, 5dB and 10dB, respectively.

bottom is equally significant (see Fig. 9(b)), and (iii) thermal information of the crack tip is more conspicuous than that at the bottom (see Fig. 9(c)). These imply that the use of the prominent features can directly locate as well as measure the size of the crack.

Independent Component Analysis (ICA) [14] is used to process the raw thermo-images and the pre-segmentation image is shown in Fig. 10. In our work, the difference ISMs and the proposed method have been carried out on Fig. 10, and the segmentation results are shown in Table II.

In Table II, it is clearly seen that, Hamadani yields worse segmentation results than Otsu, IT, RG and FOSP-GA, which are seriously contaminated by background. In the simulation work, Otsu, IT, RG and FOSP-GA have produced high segmentation quality where the target (i.e. crack) is effectively separated from the background for all the tested patterns, that is, crack tips are obtained for TP I, crack bottoms are obtained for TP III, and both tips and bottoms are acquired for TP II.

With regards to the FOSP-GA, the evolution curves have been shown in Fig. 11. The curve converges to a steady state when the genetic algebra is about 17 in TP I. The corresponding histogram is divided into 6 groups, and the

mean value of the fourth group is used as threshold based on FOSP-GA estimation. For TP II and TP III, the genetic algebras are about 10 and 13 in the steady state of the evolution curves, respectively. In addition, the histogram is divided into 4 and 5 groups, and the average of the third and fourth group is chosen as threshold, respectively. It is noted that the resulted group number is different for various TP tests, which signifies the adaptive behavior of the FOSP-GA to render optimal performance. In addition, 50 generations have been used and shown to be adequate for the tested TPs.

In Table II, it is shown that the difference of threshold selection directly affects the accuracy of image segmentation. In Fig. 12, the distribution of thresholds are presented in image histograms. For Hamadani, IT, Otsu and FOSP-GA, threshold is selected as 2.9001, 2.9012, 2.9013 and 2.9024 in TP I; 5.1771, 5.1781, 5.1784 and 5.1787 are selected in TP II; 3.4604, 3.4625, 3.4649 and 3.4658 are selected in TP III, respectively. Regarding the quality of segmentation of thermal images, as the target locates at the top-end of the histogram, the closer the threshold is to the range of the top-end of the histogram, the more accurate is the target separation. As for Hamadani, the threshold is located far from the top-end of the histogram and this has led to lower segmentation performance.

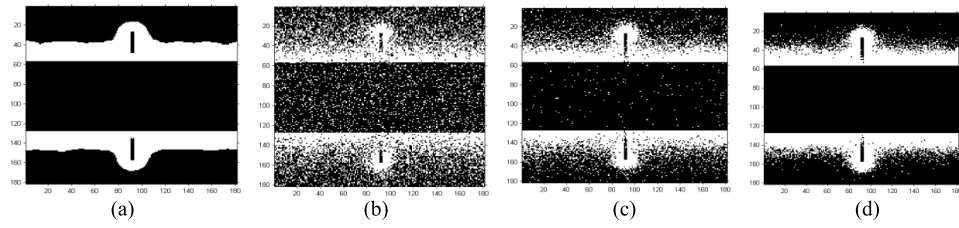


Fig. 17. (a) segmentation result by Otsu of pre-segmented image; (b)-(d) segmentation results by Otsu of pre-segmented image with white noise of 0dB, 5dB and 10dB, respectively.

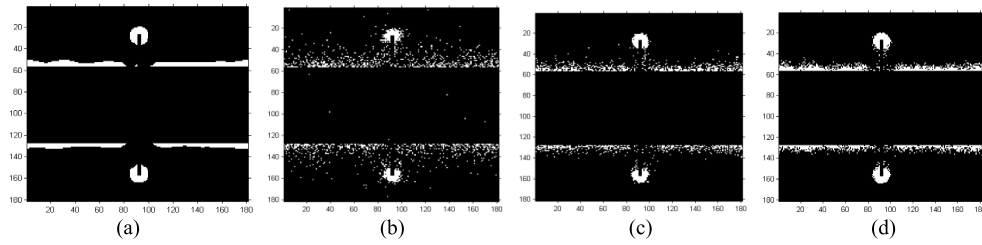


Fig. 18. (a) segmentation result by K-Means of pre-segmented image; (b)-(d) segmentation results by K-Means of pre-segmented image with white noise of 0dB, 5dB and 10dB, respectively.

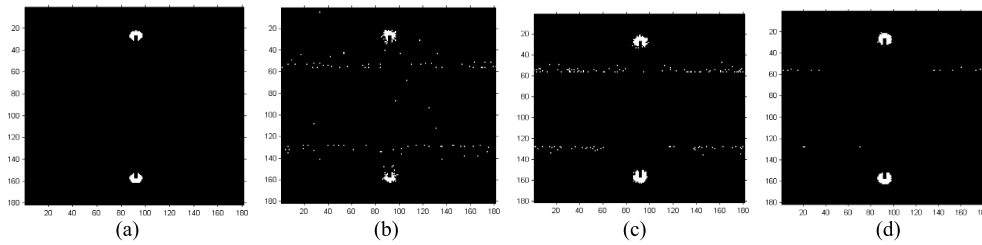


Fig. 19. (a) segmentation result by RG of pre-segmented image; (b)-(d) segmentation results by RG of pre-segmented image with white noise of 0dB, 5dB and 10dB, respectively.

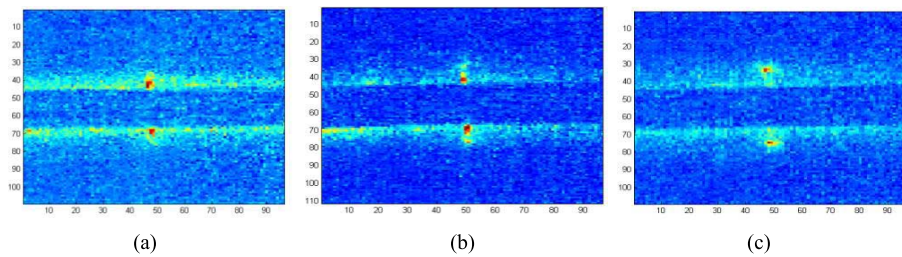


Fig. 20. (a)-(c) Thermal patterns in the real experiments.

However, the threshold obtained from the proposed methods are closer to the end of the histogram, and this results in higher accuracy in target segmentation.

In addition, K-means and the region growing (RG) methods have been implemented on the result of Fig. 10, the corresponding segmentation results are shown in Table II. To perform an objective evaluation for various ISMs, F-Score is computed in Table III. According to Table III, it is shown that the F-Scores of Hamadani and K-means are the worst while the F-Scores of Otsu and IT attain higher values but the best performance is actually rendered by RG and FOSP-GA. As for the RG method, however, human intervention is required to determine the selection of region seeds. This ambiguous case prevents the use of this method in automated environments. Differences of the F-Score from various methods are not

significant according to Table III. In the simulation work, most methods show a relatively good performance in segmenting the target defect. The reasons can be attributed to: 1) no interference from background of coil in simulation study; 2) no interference from surface condition of the test sample in simulation study; 3) no interference from environment; 4) no interference from non-uniform heating. However, above assumptions deviate considerably in real experimental study where the images are subject to unknown interference.

In order to objectively illustrate the time cost of the algorithms, Otsu, IT, Hamadani, K-Means, RG and FOSP-GA are carried out under the same operating environment (Processor: Intel(R) Xeon(R) CPU E5-2650 2.00 GHZ; RAM: 64.0 GB), the results are shown in Table IV. As shown in Table IV, the proposed FOSP-GA and RG cost longer time than other

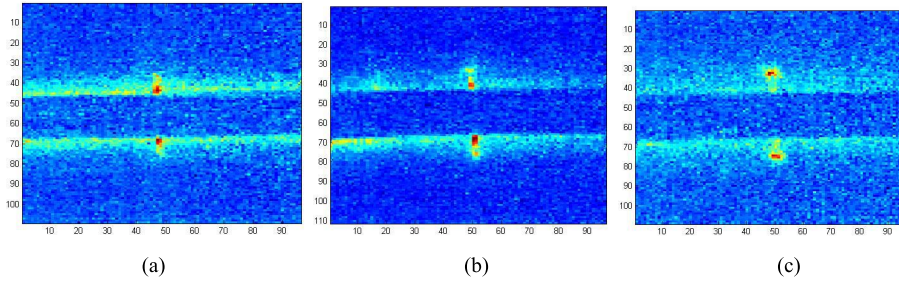


Fig. 21. (a)-(c) The corresponding pre-segmented images of Fig. 23(a)-(c).

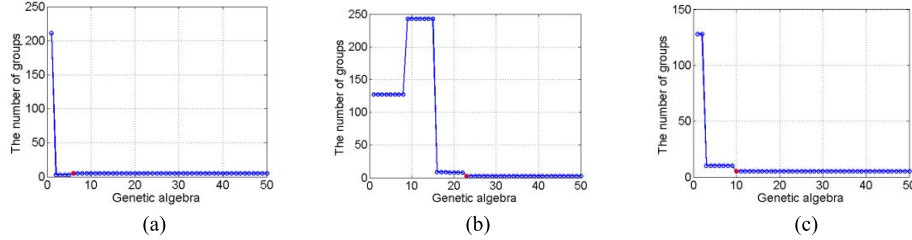


Fig. 22. (a)-(c) Evolution curve of FOSP-GA for TP I, II, III, respectively in the experiment.

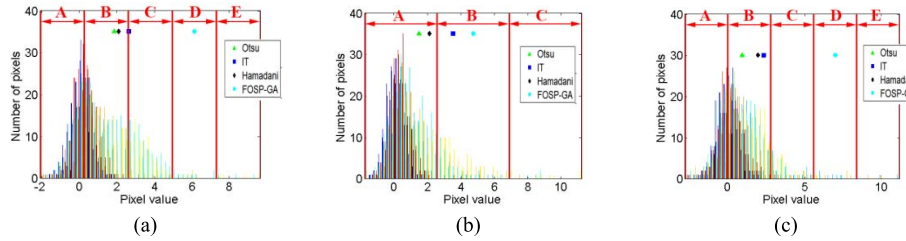


Fig. 23. (a)-(c) Histogram for TP I, II, III, respectively in the experiment.

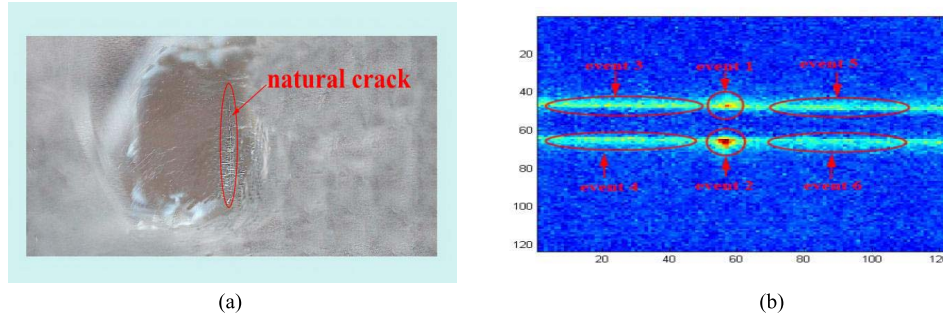


Fig. 24. (a) Natural crack, (b) pre-segmented image.

TABLE IV
RUNTIME COMPARISON (s)

method	simulation			
	TP I	TP II	TP III	average
Otsu	1.846	1.212	1.091	3.383
IT	0.038	0.041	0.054	0.044
Hamadani	0.045	0.042	0.036	0.041
K-Means	0.245	0.278	0.261	0.410
RG	5.001	4.823	4.321	4.715
FOSP-GA	4.108	4.216	4.214	4.179

methods. However, the accuracy of defect inspection is one of the primary important tasks for industrial applications. The cost time of the proposed method is acceptable while the detection performance has been significantly improved.

2) *Anti-Noise Verification*: In order to validate the segmentation performance under different controlled level of noise, a relatively good thermal image is artificially selected

(i.e. TP III), as shown in Fig. 13(a). In order to assess the de-noising capabilities, different level of white noise (0dB, 5dB and 10dB) are added to the pre-segmentation image, as shown in Fig. 13(b)-(d). The proposed method FOSP-GA is used to process Fig. 13(a)-(d), and the segmentation results are shown in Fig. 14. As shown in Fig. 14, the crack tip areas are effectively separated from the background. Even though different level of noise is added to the image, the defect area can still be segmented from background. However other methods show relatively inferior detection performance as noted by the inclusion different variabilities of the background in segmentation results, as shown in Figs. 15 - 19.

3) *Experimental Validation*: Fig. 9 shows simulation studies of three TPs and the corresponding experiment images are shown in Fig. 20(a), (b) and (c), respectively. The prominent features of the crack have been detected, i.e. the heating of the bottom is more significant (see Fig. 20(a)), the heating of the tip dominants (see Fig. 20(c)), and both positions

TABLE V
SEGMENTATION RESULTS OF VARIOUS METHODS IN THE EXPERIMENT

	TP I	TP II	TP III
Otsu			
IT			
Hamadani			
FOSP-GA			
K-Means			
RG			

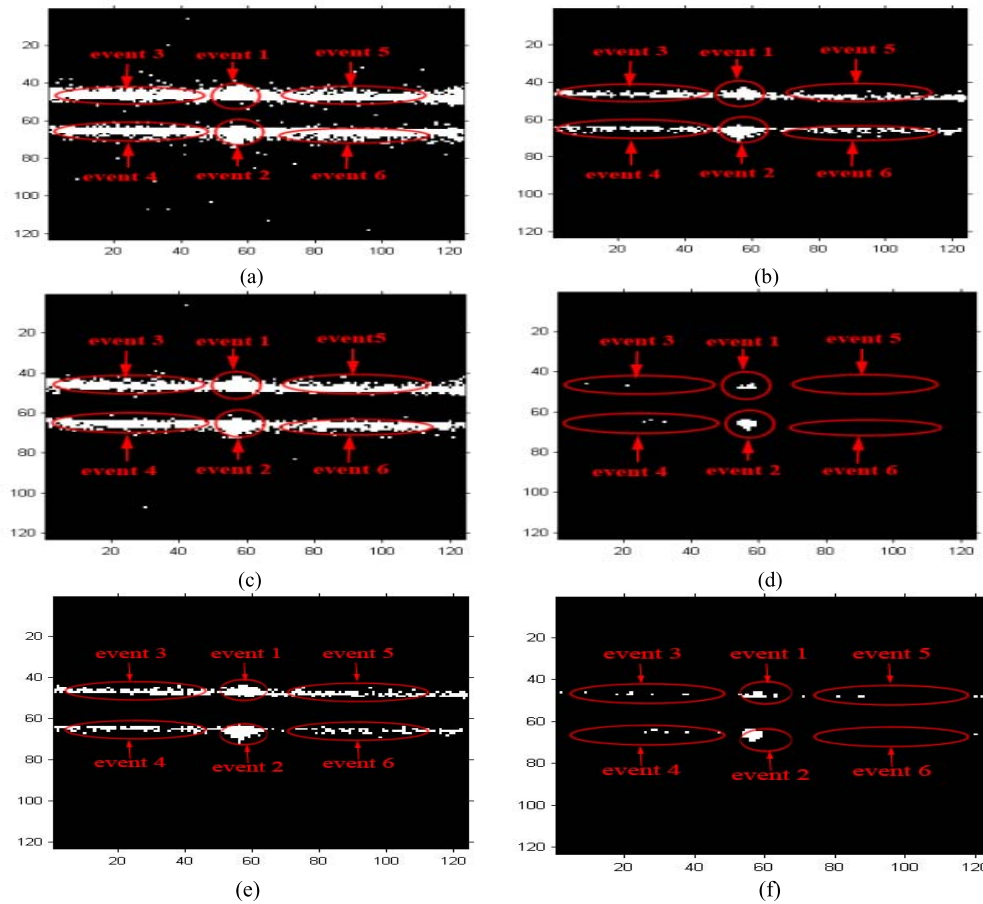


Fig. 25. (a)-(f) Segmentation results of Otsu, IT, Hamadani, FOSP-GA, K-Means and RG.

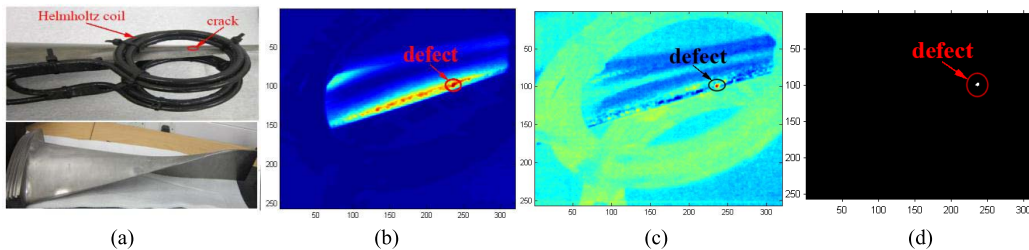


Fig. 26. (a) Turbine blade with thermal fatigue natural crack; (b) the original thermal image of (a); (c) pre-segmented image; (d) segmentation result by FOSP-GA.

dominant (see Fig. 20(b)). However, there are differences between Fig. 9 and Fig. 20.

These are due to several impact factors such as sensitivity of the camera, the effects of environmental noise and error introduced in the experiments. Otsu, IT, Hamadani K-Means, RG and FOSP-GA are used for segmentation and the results are shown in Table V. The corresponding F-Scores have been computed in Table VI. The experiment results illustrate that the proposed method provides significant improvement and performs better than others. It is remarkable that the results from Otsu and IT in the experiment study are not as ideal as with the simulation results, and have led low values of the F-Scores. The mean F-Scores of Otsu and IT are reduced by 89.05% and 74.4%, respectively, compared to the mean F-scores of the simulation. The main reason for this phenomenon is attributed

to the environmental noise in the experiment and the factor of uneven distribution of heating. Otsu, IT and Hamadani methods are vulnerable to background interference in ECPT experiments. So far only the RG and the proposed method perform more robustly in the presence of interference, and significant emphasis is placed on the achievement of uneven excitation that is available depressed. In Fig. 22, the evolution curves have reached the steady state with the genetic algebras equal to 6, 23 and 10 for TP I, II and III, respectively. The corresponding histograms are divided into 5, 3 and 5 groups, respectively. In addition, the thresholds are adapted to 6.1133, 4.7207 and 6.9995, which are approaching the top-end of the histogram that fall in the target area (see Fig. 23). Thus, defects can be accurately segmented based on FOSP-GA. On the other hand, Fig. 23 shows that the thresholds of Otsu,

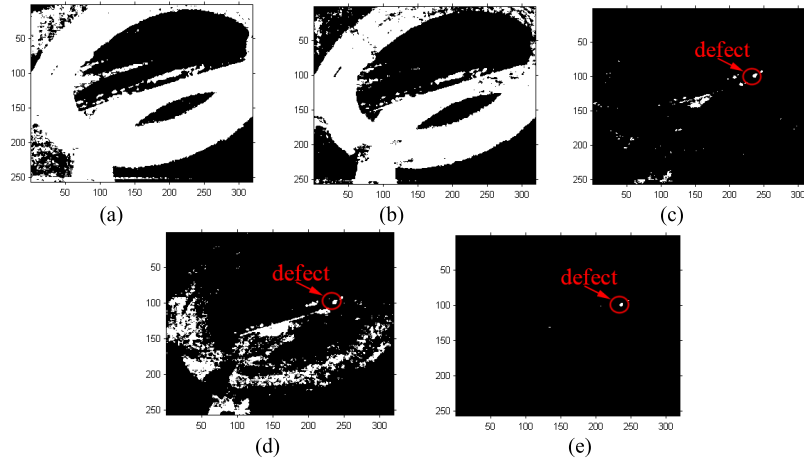


Fig. 27. (a)-(e) The segmentation results of Figure 8(c) by using Otsu, IT, Hamadani, K-Means and RG, respectively.

TABLE VI
F-SCORE FOR VARIOUS ISMs IN THE EXPERIMENT

	Experiment			
	TP I	TP II	TP III	average
Otsu	0.0400	0.0506	0.0245	0.0384
IT	0.1020	0.3134	0.1417	0.1857
Hamadani	0.0649	0.0879	0.0868	0.0799
K-Means	0.1207	0.0689	0.1398	0.1098
RG	0.4019	0.6658	0.8010	0.6229
FOSP-GA	0.4783	0.6667	0.8947	0.6799

TABLE VII
RUNTIME COMPARISON (s)

	Experiment			
	TP I	TP II	TP III	average
Otsu	0.683	0.742	0.643	0.689
IT	0.109	0.114	0.111	0.111
Hamadani	0.112	0.110	0.101	0.108
K-Means	0.689	0.623	0.598	0.609
RG	3.012	3.100	3.198	3.103
FOSP-GA	3.140	2.812	2.928	2.960

IT and Hamadani are far from the terminal region of the histogram. These are 1.8544, 2.6255 and 2.0844 for TP I, 1.4972, 3.5052 and 2.1182 for TP II, 0.9783, 2.3722 and 1.9983 for TP III, respectively. In Table VI, the mean F-Scores of FOSP-GA have been improved by 64.15%, 49.42%, 60%, 57.01% and 5.7% compared to Otsu, IT, Hamadani, K-Means and RG, respectively. It is very evident that the FOSP-GA provides a significant improvement and delivers the best result for extracting the target for stimulated thermal image, and this finding is in agreement with the simulation.

The time cost of the algorithms has been computed and the results are shown in Table VII. The proposed method FOSP-GA and RG consume longer time than other methods while FOSP-GA is able to effectively improve the detection performance.

More validation studies of natural cracks with complex geometries are tested based on ECPT. In Fig. 24(a), a natural crack (i.e. ellipse marked area) is generated by intergranular corrosion in nuclear industry material. The pre-segmented image is acquired and shown in Fig. 24(b). Otsu,

TABLE VIII
SEGMENTATION PERFORMANCE ANALYSIS

	Otsu	IT	Hamadani	K-Means	RG	FOSP-GA
TPR	1	1	1	1	1	1
FPR	2/3	2/3	2/3	2/3	3/5	1/2

IT, Hamadani, K-Means, RG and FOSP-GA have been used to segment the natural crack related to the thermal pattern, and the results are shown in Fig. 25.

As the F-Score is a pixel level evaluation index, however, it is difficult to calibrate ground truth of natural crack. The evaluation index based on region is used to evaluate the segmentation quality of natural crack. The segmented image from different segmentation algorithms are compared to their corresponding ground truth image. The performance and accuracy of segmentation methods are evaluated based on parameters of true positive rate (TPR), false positive rate (FPR). In order to assess the accuracy of image segmentation, the value of TPR and FPR are calculated using $TPR = TP/(TP+FN)$ and $FPR = FP/(TP+FP)$. An accurate segmentation result should have TPR closes to 1, while FPR should be as low as possible [39]. Raw thermal image or pre-segmented image from ICA can be regarded as ground truth, defect and background are considered as various events to carry out the examination of the overlapping. Defects are considered as event1 and event2, i.e. ellipse marking area of Fig. 24(b). Table VIII shows the comparison of segmentation performance.

According to TPR in Table VIII, it can be seen that defects are detected by the six methods. However, Otsu, IT, Hamadani, K-Means and RG provide higher FPR than FOSP-GA, which interprets the FOSP-GA performs the best segmentation results in overall.

In addition, a test specimen of a turbine blade with a thermal fatigue natural crack is used to evaluate the performance of FOSP-GA and this is shown in Fig. 26(a). In this study, a helmholtz coil is chosen as the excitation coil. This is a different type of coil compared to the line coil. The placement of the coil is shown in Fig. 26(a) and it will excite the whole region under the circle. An original thermal image is shown in Fig. 26(b). It is difficult to distinguish the defect if the location of defect is unknown in advance, and the real defect is not easy to be judged in the original thermal image. ICA is used to process the original thermography sequence to extract

the defect information and eliminate false positives. The pre-segmentation image is shown in Fig. 26(c). Furthermore, this image is subsequently processed by the FOSP-GA whose segmentation result is shown in Fig. 26(d).

In addition, Otsu, IT, Hamadani, K-Means and RG method are used for comparison as shown in Figure 26(c). The results are shown in Fig. 27 where the presence of different levels of background interference. The background interference is especially serious for results from Otsu, IT Hamadani and K-Means. The RG shows the better results as it has reduced the most of the unwanted interference. However, comparing Fig. 26(d) and Fig. 27, the proposed method FOSP-GA still outperformed other methods.

IV. CONCLUSION AND FUTURE WORK

This paper has proposed a physics-based FOSP-GA image segmentation method to quantitatively analyze defects for application in inductive thermography imaging. The segmentation threshold is determined based on the FOSP, and GA is applied to automatically determine the optimal statistical feature and the threshold selection. Quantitative defect detectability is objectively assessed and compared with Otsu, IT, Hamadani, K-means and RG by using global evaluation F-Score. The obtained results from conducted experimental studies have consistently shown that the proposed FOSP-GA has outperformed other segmentation methods. It has accurately segmented the defects from background and effectively inhibited the influences of uneven excitation and noise. The work can be further applied to other types of defects detection and quantitative evaluation such as the inspection of fatigue crack on steel blade for automated visual inspection of defects.

REFERENCES

- [1] C. E. Betz, *Principles of Magnetic Particle Testing*. Columbus, OH, USA: American Society for Nondestructive Testing, 1985, p. 234.
- [2] B. W. Drinkwater and P. D. Wilcox, "Ultrasonic arrays for non-destructive evaluation: A review," *NDT E Int.*, vol. 39, no. 7, pp. 525–541, 2006.
- [3] E. Z. Kordatos, D. G. Aggelis, and T. E. Matikas, "Monitoring mechanical damage in structural materials using complimentary NDE techniques based on thermography and acoustic emission," *Compos. B, Eng.*, vol. 43, no. 6, pp. 2676–2686, 2012.
- [4] B. Gao, H. Zhang, W. L. Woo, G. Y. Tian, L. Bai, and A. Yin, "Smooth nonnegative matrix factorization for defect detection using microwave non-destructive testing and evaluation," *IEEE Trans. Instrum. Meas.*, vol. 63, no. 4, pp. 923–934, Apr. 2014.
- [5] M. Ishikawa, H. Hatta, Y. Habuka, R. Fukui, and S. Utsunomiya, "Detecting deeper defects using pulse phase thermography," *Infr. Phys. Technol.*, vol. 57, pp. 42–49, Mar. 2013.
- [6] N. P. Avdelidis, B. C. Hawtin, and D. P. Almond, "Transient thermography in the assessment of defects of aircraft composites," *NDT E Int.*, vol. 36, no. 6, pp. 433–439, 2003.
- [7] V. P. Vavilov and D. D. Burleigh, "Review of pulsed thermal NDT: Physical principles, theory and data processing," *NDT E Int.*, vol. 73, pp. 28–52, Jul. 2015.
- [8] B. B. Lahiri, S. Bagavathiappan, P. R. Reshmi, J. Philip, T. Jayakumar, and B. Raj, "Quantification of defects in composites and rubber materials using active thermography," *Infr. Phys. Technol.*, vol. 55, nos. 2–3, pp. 191–199, 2012.
- [9] J. Wilson, G. Y. Tian, I. Z. Abidin, S. Yang, and D. Almond, "Pulsed eddy current thermography: System development and evaluation," *Insight - Non-Destruct. Test. Condition Monitor.*, vol. 52, no. 2, pp. 87–90, 2010.
- [10] I. Z. Abidin, G. Y. Tian, J. Wilson, S. Yang, and D. Almond, "Quantitative evaluation of angular defects by pulsed eddy current thermography," *NDT E Int.*, vol. 43, no. 7, pp. 537–546, 2010.
- [11] M. Grenier, C. Ibarra, and X. Maldague, "Development of a hybrid non-destructive inspection system combining induction thermography and eddy current technique," *Quant. Infr. Thermogr.*, vol. 43, no. 5, pp. 318–321, 2010.
- [12] L. Cheng and G. Y. Tian, "Surface crack detection for carbon fiber reinforced plastic (CFRP) materials using pulsed eddy current thermography," *IEEE Sensors J.*, vol. 11, no. 12, pp. 3261–3268, Dec. 2011.
- [13] J. Wilson, G. Tian, I. Mukriz, and D. Almond, "PEC thermography for imaging multiple cracks from rolling contact fatigue," *NDT E Int.*, vol. 44, no. 6, pp. 505–512, 2011.
- [14] B. Gao, L. Bai, W. L. Woo, G. Y. Tian, and Y. Cheng, "Automatic defect identification of eddy current pulsed thermography using single channel blind source separation," *IEEE Trans. Instrum. Meas.*, vol. 63, no. 4, pp. 913–922, Apr. 2014.
- [15] M. Pan, Y. Z. He, G. Y. Tian, D. Chen, and F. Luo, "Defect characterisation using pulsed eddy current thermography under transmission mode and NDT applications," *NDT E Int.*, vol. 52, pp. 28–36, Nov. 2012.
- [16] J. Liu *et al.*, "Nondestructive evaluation of early contact fatigue using eddy current pulsed thermography," *IEEE Sensors J.*, vol. 15, no. 8, pp. 4409–4419, Aug. 2015.
- [17] Y. A. Plotnikov and W. P. Winfree, "Advanced image processing for defect visualization in infrared thermography," *Proc. SPIE*, vol. 3361, 1999.
- [18] R. C. Gonzalez and R. E. Woods, *Digital Image Processing*. Beijing, China: Publishing House of Electronic Industry, Jun. 2011, pp. 443–444.
- [19] S. K. Mylonas, D. G. Stavrakoudis, J. B. Theocharis, G. C. Zalidis, and I. Z. Gitas, "A local search-based GeneSIS algorithm for the segmentation and classification of remote-sensing images," *IEEE J. Sel. Topics Appl. Earth Observat. Remote Sens.*, vol. 9, no. 4, pp. 1470–1492, Apr. 2016.
- [20] J. S. Hernandez, E. M. Izquierdo, and A. A. Hidalgo, "Improving parameters selection of a seeded region growing method for multi-band image segmentation," *IEEE Latin Amer. Trans.*, vol. 13, no. 3, pp. 843–849, Mar. 2015.
- [21] X. Liu, Q. Xu, J. Ma, H. Jin, and Y. Zhang, "MsLRR: A unified multiscale low-rank representation for image segmentation," *IEEE Trans. Image Process.*, vol. 23, no. 5, pp. 2159–2167, May 2014.
- [22] M. Jian and C. Jung, "Interactive image segmentation using adaptive constraint propagation," *IEEE Trans. Image Process.*, vol. 25, no. 3, pp. 1301–1311, Mar. 2016.
- [23] J. Wang and W. Huang, "Image segmentation with eigenfunctions of an anisotropic diffusion operator," *IEEE Trans. Image Process.*, vol. 25, no. 5, pp. 2155–2167, May 2016.
- [24] B. Hell, M. Kassubeck, P. Bauszat, M. Eisemann, and M. Magnor, "An approach toward fast gradient-based image segmentation," *IEEE Trans. Image Process.*, vol. 24, no. 9, pp. 2633–2645, Sep. 2015.
- [25] X. Wang, Y. Tang, S. Masnou, and L. Chen, "A global/local affinity graph for image segmentation," *IEEE Trans. Image Process.*, vol. 24, no. 4, pp. 1399–1411, Apr. 2015.
- [26] G. Liu, Y. Zhang, and A. Wang, "Incorporating adaptive local information into fuzzy clustering for image segmentation," *IEEE Trans. Image Process.*, vol. 24, no. 11, pp. 3990–4000, Nov. 2015.
- [27] N. Y. El-Zehiry and L. Grady, "Contrast driven elastica for image segmentation," *IEEE Trans. Image Process.*, vol. 25, no. 6, pp. 2508–2518, Jun. 2016.
- [28] X. P. Dong, J. B. Shen, Ling Shao, and L. van Gool, "Sub-Markov random walk for image segmentation," *IEEE Trans. Image Process.*, vol. 25, no. 2, pp. 516–527, Feb. 2016.
- [29] X. Li, H. Jiang, and G. Yin, "Detection of surface crack defects on ferrite magnetic tile," *NDT E Int.*, vol. 62, pp. 6–13, Mar. 2014.
- [30] H. Li, Y. Tan, and Y. S. Li, "Image layering based small infrared target detection method," *Electron. Lett.*, vol. 50, no. 1, pp. 42–44, 2014.
- [31] R. świta and Z. Suszyński, "Cluster segmentation of thermal image sequences using kd-tree structure," *Int. J. Thermophys.*, vol. 35, no. 12, pp. 2374–2387, 2014.
- [32] Y. Huang and J.-W. Wu, "Infrared thermal image segmentations employing the multilayer level set method for non-destructive evaluation of layered structures," *NDT E Int.*, vol. 43, no. 1, pp. 34–44, 2010.
- [33] N. Otsu, "A threshold selection method from gray-level histograms," *Automatica*, vol. 11, nos. 285–296, pp. 23–27, 1975.
- [34] W. H. Richardson, "Bayesian-based iterative method of image restoration," *J. Soc. Amer.*, vol. 62, no. 1, pp. 55–59, 1972.
- [35] N. A. Hamadani, "Automatic target cueing in IR imagery," Air Force Inst. Technol., Wright-Patterson Air Force Base, OH, USA, Tech. Rep., 1981.

- [36] A. Z. Chitade and S. K. Katiyar, "Colour based image segmentation using K-means clustering," *Int. J. Eng. Sci. Technol.*, vol. 2, no. 10, pp. 5319–5325, 2010.
- [37] J. Wilson, G. Y. Tian, I. Z. Abidin, S. Yang, and D. Almond, "Modelling and evaluation of eddy current stimulated thermography," *Nondestruct. Test. Eval.*, vol. 25, no. 3, pp. 205–218, 2010.
- [38] D. E. Goldberg and J. H. Holland, "Genetic algorithms and machine learning," *Mach. Learn.*, vol. 3, nos. 2–3, pp. 95–99, 1988.
- [39] D. Mery and F. Pedreschi, "Segmentation of colour food images using a robust algorithm," *J. Food Eng.*, vol. 66, no. 3, pp. 353–360, 2005.
- [40] D. Davies, P. Palmer, and M. Mirmehdi, "Robust tracker of small, fast-moving low-contrast targets," in *Proc. Eur. Signal Process. Conf.*, vol. 3, Sep. 1998, pp. 1–4.
- [41] J. Schmidhuber, "Deep learning in neural networks: An overview," *Neural Netw.*, vol. 61, pp. 85–117, Jan. 2015.



Bin Gao (M'12–SM'14) received the B.Sc. degree in communications and signal processing from Southwest Jiao Tong University, China, in 2005, and the M.Sc. degree (Hons.) in communications and signal processing and the Ph.D. degree from Newcastle University, U.K., in 2008 and 2011, respectively. From 2011 to 2013, he was a Research Associate with Newcastle University, where he was involved in wearable acoustic sensor technology. He is currently a Professor with the School of Automation Engineering, University of Electronic

Science and Technology of China, China. He has authored over 60 papers on these topics on various journals and international conference proceedings. His research interests include sensor signal processing, machine learning, social signal processing, nondestructive testing, and evaluation, where he actively publishes in these areas. He has coordinated several research projects from the National Natural Science Foundation of China.



Xiaoqing Li received the B.Sc. degree from the School of Life Information and Instrument Engineering, Hangzhou Dianzi University, Hangzhou, China, in 2010. She is currently pursuing the M.Sc. degree in quantitative analysis and evaluation for surface cracks using electromagnetic technique with the University of Electronic Science and Technology of China, Chengdu, China. Her research interests include sensor signal processing, feature extraction, image segmentation, and thermography nondestructive testing.



Wai Lok Woo received the B.Eng. degree (Hons.) in electrical and electronics engineering and the Ph.D. degree from Newcastle University, U.K. He was awarded the IEE Prize and the British Scholarship to continue his research work. He is currently a Senior Lecturer and the Director of Operations with the School of Electrical and Electronic Engineering. His major research is in the mathematical theory and algorithms for nonlinear signal and image processing. This includes the areas of machine learning for signal processing, blind source separation, multidimensional signal processing, and signal/image deconvolution and restoration.

He has an extensive portfolio of relevant research supported by a variety of funding agencies. He has authored over 250 papers on these topics on various journals and international conference proceedings. He is currently an Associate Editor of several international journals and has served as a lead-editor of journals' special issues.



Gui Yun Tian (M'01–SM'03) received the B.Sc. degree in metrology and instrumentation and the M.Sc. degree in precision engineering from the University of Sichuan, Chengdu, China, in 1985 and 1988, respectively, and the Ph.D. degree from the University of Derby, Derby, U.K., in 1998. From 2000 to 2006, he was a Lecturer, a Senior Lecturer, a Reader, a Professor, and the Head of the Group of Systems Engineering, respectively, with the University of Huddersfield, U.K. Since 2007, he has been at Newcastle University, Newcastle upon Tyne,

U.K., where he has been the Chair Professor in sensor technologies. He is currently an Adjunct Professor with the School of Automation Engineering, University of Electronic Science and Technology of China. He has coordinated several research projects from the Engineering and Physical Sciences Research Council, Royal Academy of Engineering and FP7, on top of this he also has good collaboration with leading industrial companies, such as Airbus, Rolls Royce, BP, nPower, Networkrail, and TWI.